Environmental Science and Ecotechnology 15 (2023) 100244

Contents lists available at ScienceDirect

Environmental Science and Ecotechnology

journal homepage: www.journals.elsevier.com/environmental-science-and-ecotechnology/

Original Research

A tailored and rapid approach for ozonation catalyst design

Min Li [a, b, 1], Liya Fu [a, b, 1], Liyan Deng [a, b], Yingming Hu [a, b, c], Yue Yuan [a, b], Changyong Wu [a, b, *]

[a] State Key Laboratory of Environmental Criteria and Risk Assessment, Chinese Research Academy of Environment Sciences, Beijing, 100012, China
[b] Research Center of Water Pollution Control Technology, Chinese Research Academy of Environment Sciences, Beijing, 100012, China
[c] College of Urban and Environment Science, Northwest University, Xi'an, 710127, China

ARTICLE INFO

Article history:
Received 30 September 2022
Received in revised form
2 February 2023
Accepted 3 February 2023

Keywords:
Machine learning
Ozonation catalyst
Fluorescence spectroscopy
Artificial neural network
Catalytic ozonation

ABSTRACT

Catalytic ozonation is widely employed in advanced wastewater treatment owing to its high mineralization of refractory organics. The key to high mineralization is the compatibility between catalyst formulation and wastewater quality. Machine learning can greatly improve experimental efficiency, while fluorescence data can provide additional wastewater quality information on the composition and concentration of organics, which is conducive to optimizing catalyst formulation. In this study, machine learning combined with fluorescence spectroscopy was applied to develop ozonation catalysts (Mn/γ-Al_2O_3 catalyst was used as an example). Based on the data collected from 52 different catalysts, a machine-learning model was established to predict catalyst performance. The correlation coefficient between the experimental and model-predicted values was 0.9659, demonstrating the robustness and good generalization ability of the model. The range of the catalyst formulations was preliminarily screened by fluorescence spectroscopy. When the wastewater was dominated by tryptophan-like and soluble microbial products, the impregnation concentration and time of $Mn(NO_3)_2$ were less than 0.3 mol L^{-1} and 10 h, respectively. Furthermore, the optimized Mn/γ-Al_2O_3 formulation obtained by the model was impregnation with 0.155 mol L^{-1} $Mn(NO_3)_2$ solution for 8.5 h and calcination at 600 °C for 3.5 h. The model-predicted and experimental values for total organic carbon removal were 54.48% and 53.96%, respectively. Finally, the improved catalytic performance was attributed to the synergistic effect of oxidation (•OH and $^1O_2$) and the Mn/γ-Al_2O_3 catalyst. This study provides a rapid approach to catalyst design based on the characteristics of wastewater quality using machine learning combined with fluorescence spectroscopy.

1. Introduction

With the rapid development of industrial processes, most industrial wastewater remains refractory after the biochemical stage because it contains many toxic substances (such as benzene, aldehydes, and phenols) [1]. Recently, the discharge standards of industrial wastewater have become increasingly strict. Advanced oxidation processes mineralize refractory organics in wastewater through the reaction of strong oxidation radicals in the system, including ozonation, photocatalytic, Fenton, and sulfate radical-based reactions [2,3]. Catalytic ozonation has shown promise for treating refractory organic substances by promoting the decomposition of ozone (O_3) molecules into free radicals (•OH, $^1O_2$, $•O_2^-$) with a higher redox potential using catalysts [4,5]. Compared with pure ozonation, the use of catalysts can enhance the removal efficiency through electrostatic interaction or hydrogen bonding adsorption of organic matter [6,7]. Therefore, catalysts play an important role in the catalytic ozonation process for refractory wastewater treatment. However, previous studies have mainly focused on developing catalysts with high activity, while ignoring the corresponding water quality characteristics.

Catalyst activity is closely related to the characteristics of organic matter in wastewater, with the degradation efficiency of the same catalyst varying greatly for different organic matter. For

* Corresponding author. State Key Laboratory of Environmental Criteria and Risk Assessment, Chinese Research Academy of Environment Sciences, Beijing, 100012, China.
E-mail address: wucy@craes.org.cn (C. Wu).
[1] These authors contributed equally to this work and should be considered co-first authors.

https://doi.org/10.1016/j.ese.2023.100244

the catalytic ozonation process using MnO_2 catalyst, the degradation efficiencies for phenol, hydroquinone, *p*-nitrophenol (4-NP), and *p*-chlorophenol were 76.1%, 91.9%, 97%, and 100%, respectively [8,9]. This indicated that hydroquinone, 4-NP, and *p*-chlorophenol were more easily degraded than phenol. Similarly, different metal oxide catalysts can affect the degradation efficiency of the same organic matter in the catalytic ozonation process. For phenol degradation using the catalytic ozonation process, the removal efficiencies with MnO_2, Mn_2O_3, Mn_3O_4, Mn/γ-Al_2O_3, and CeO_2 supported on carbon nanotubes as catalysts were 76.1%, 66.8%, 58.4%, 82.6%, and 96%, respectively [9–11]. In summary, owing to the intricate characteristics of wastewater, complex interactions among influent quality indexes and catalyst formulations should be considered during catalyst optimization. Traditional catalyst optimization methods are time-consuming and costly, as the optimized catalyst is usually obtained via multiple experiments to adjust the catalyst formulation based on the possible mechanism. Therefore, new methods that can optimize the catalyst formulation more quickly need to be developed.

In recent years, machine learning has undergone rapid development in environmental, biological, and chemical fields to reduce blind trials and improve experimental efficiency. Burger et al. [12] introduced a Bayesian algorithm in machine learning to achieve 688 experiments in eight days, and identified an optimal photocatalyst for hydrogen production that was six times more active than the original formula. Among various machine learning methods, the artificial neural network (ANN) model can use predictive data to investigate the nonlinear correlation of process parameters for modeling, rapidly learning from data and finding the optimal solution to a problem [13]. The ANN model has been extensively applied to evaluate traditional catalytic processes and catalyst design. A prediction of catalyst activity in the Fischer–Tropsch synthesis used the catalyst carrier, active phase, and promoters as inputs for the ANN model [13]. The best ANN model for predicting hydrogen production efficiency was established under different operating conditions, including reaction temperature, $NaBH_4$ concentration, and catalyst loading [14]. Catalyst deactivation during the production of synthesis gas by methane dry reforming was introduced into an ANN model by Alsaffar et al. [15]. The reactions in the above research are relatively simple with relatively stable conditions. However, the degradation of organic matter by the catalytic ozonation process is difficult to explore owing to the complexity of wastewater quality and the variability of the water–gas–solid three-phase reaction system. Furthermore, the ANN model has not been utilized to optimize ozonation catalysts in the wastewater treatment field with complex reaction conditions.

Fluorescence spectroscopy, in which light is absorbed and the energy is re-emitted as fluorescence, can be applied to determine wastewater quality due to its fingerprint characteristics. Fluorescence data can quantify dissolved organic matter (DOM) [16,17], and provide information on the composition and concentration of DOM removed and transformed by wastewater treatment, in which traditional water quality parameters are inadequate [18,19]. Fluorescence spectroscopy has the advantages of fast measurement, high sensitivity and selectivity, and limited requirements for sample pretreatment [18,20]. Therefore, fluorescence spectroscopy techniques have recently been increasingly used to monitor DOM in wastewater treatments. However, fluorescence spectroscopy have never been coupled with the ANN model to optimize the catalyst formulation.

This study aimed to evaluate the effect of ANN input variables on the performance of ozonation catalysts, including catalyst formulation and influent quality indexes, optimize catalyst formulation using the ANN model combined with fluorescence spectroscopy, and demonstrate the synergistic effect of oxidation (•OH and $^1O_2$) and the Mn/γ-Al_2O_3 catalyst on improving catalytic performance. The application of the ANN model in this study was anticipated to stimulate an understanding of the compatibility between complex wastewater quality and catalyst preparation. Furthermore, the ANN model combined with fluorescence spectroscopy can be used as an effective strategy to provide experience for further development, performance prediction, and process simulation of catalysts in complex wastewater systems.

2. Materials and methods

2.1. Original wastewater

The petrochemical secondary effluent (PSE) used as the original wastewater in this study was obtained from the effluent of the sedimentation tank at a typical petrochemical-integrated wastewater treatment plant in northern China. The wastewater treatment plant, which has a capacity of 5000 $m^3\ h^{-1}$, treats influent from over 70 sources. The plant employs hydrolysis acidification–anoxic/oxic process for biochemical treatment [21]. The characteristics of PSE are shown in Table S4. The wastewater was filtered through qualitative filter paper before use.

2.2. Catalytic ozonation experiments

Catalytic ozonation treatment of wastewater with the Mn/γ-Al_2O_3 catalyst was performed in an O_3 reactor with an inner diameter of 90 mm, a height of 250 mm, and a volume of 1.59 L O_3 was generated from pure oxygen by an O_3 generator (Longevity EXT120, Beijing Tonglin, China). The O_3 concentration was controlled using a flowmeter and recorded using an online O_3 concentration detector (3S-J5000, Beijing Tonglin, China). O_3 was transported to the reactor for experiments, and the exhaust was discharged into an O_3 destroyer. Details of O_3 concentration detection are provided in Text S1 (see Supplementary information).

In each ozonation experiment, the O_3 reactor contained 1 L of PSE. For catalytic ozonation experiments, 300 g of Mn/γ-Al_2O_3 catalyst was added to the reactor. After 60 min, sodium thiosulfate was added to remove residual O_3 from the samples. The O_3 concentration was kept at 3 mg L^{-1}, and the flow rate was 200 mL min^{-1}. Each group experiment was performed in triplicate. A schematic diagram of the catalytic ozonation device is shown in Fig. S1. Detailed information on catalyst preparation and the effect of operating parameters during experiments are provided in Text S2 and Fig. S2, respectively.

2.3. Analytical methods

Total organic carbon (TOC) was determined with a TOC analyzer (TOC-$L_{CPH/CPN}$, Shimadzu, Japan), and chemical oxygen demand (COD) was determined using the potassium dichromate method. The UV absorption intensity at 254 nm (UV_{254}) was determined using a UV spectrophotometer (UV-1700, Shimadzu, Japan). The excitation emission matrix (EEM) fluorescence spectroscopy of samples was performed using a 3D-fluorescence spectrophotometer (F-7000, Hitachi, Japan) and coupled with the fluorescence regional integration (FRI) method for quantitative analysis [22]. Detailed information on the EEM determination and cumulative volume calculation is provided in Text S3.

The catalyst surface morphology (ground powder samples

scraped from the catalyst surface) was characterized by scanning electron microscopy (SEM; HITACHI SU-8010, Japan) using an accelerating voltage of 30 keV. X-ray diffraction (XRD) analysis was conducted in the 2θ range of 10°−70° with a scanning speed of 2° min^{-1}. The elemental composition of the catalyst was determined by X-ray photoelectron spectroscopy (Thermo ESCALAB 250XI XPS, USA) with 200 W Al Kα radiation (hν = 1486.6 eV). Other material characterization analysis methods are detailed in Text S4.

2.4. ANN model training

The original data were collected in catalytic ozonation experiments using 52 different catalyst formulations (Tables S5 and S6). The contributions of catalyst formulation (i.e., catalyst preparation parameters, including impregnation concentration, impregnation time, calcination temperature, and calcination time) and influent quality indexes (COD, TOC, UV_{254}, and five fluorescence region intensities) to catalyst performance were analyzed using statistical methods. Two types of 'feedforward neural network' model were developed (Fig. 1), and their prediction accuracy was compared, achieving optimal performance in the ANN model. Except for the input layer, the two ANN models had the same three-layer neural network structure, comprising the input layer, hidden layer (single layer), and output layer. In general, ANN predictive modeling involved training and testing phases, in which 44 groups were conducted as training data sets and eight groups as test data sets (sample data sets were 4, 8, 16, 20, 28, 32, 40, 48). The whole ANN model training procedure mainly comprised forward and reverse transmission. In forward transmission, the corresponding influence of input variables on the network is propagated layer by layer on the network to generate the output [23], where hyperbolic tangent transfer function tansig was adopted as the transfer function of neurons in the hidden layer (equation (1)). Owing to the error between the network output value and the actual value, the training was transferred to reverse transmission. During reverse transmission, the gradient descent technique was applied to train the weight of neurons, with the minimum error obtained after several iterations [15]. TOC removal efficiency was introduced to represent catalyst performance, and was also used as the output of the ANN model. BPANN modeling was performed using the Neural network toolkit of MATLAB 2019a, and trial-and-error testing was used to determine the model parameters [15,24]. Furthermore, the reliability of the model parameters was measured using the root mean square error (RMSE) and correlation coefficient (R^2), obtained by equations (2) and (3).

$$\text{tansig} = \frac{1 - e^{-2x}}{1 + e^{-2x}} \tag{1}$$

$$\text{RMSE} = \sqrt{\frac{1}{n}\sum_{i=1}^{n}(E_i - P_i)^2} \tag{2}$$

$$R^2 = 1 - \frac{\sum_{i=1}^{n}(P_i - E_i)}{\sum_{i=1}^{n}(E_i - \overline{E_i})^2} \tag{3}$$

where E_i is the experimental value, P_i is the predicted value of the ANN model, n is the number of training or testing samples, and $\overline{E_i}$ is the average of experimental values.

$$S_A = \frac{\sum_{i=1}^{n} V_i \frac{A_i}{\sqrt{\lambda_i}} \Big/ \sum_{i=1}^{n} V_i}{\sum_{i=1}^{m} \sum_{i=1}^{n} V_i \frac{A_i}{\sqrt{\lambda_i}} \Big/ \sum_{i=1}^{n} V_i} \tag{4}$$

where S_A is the weight of factor of index A, V_i is the variance of the principal component, A_i is the factor load matrix, and λ_i is the characteristic value.

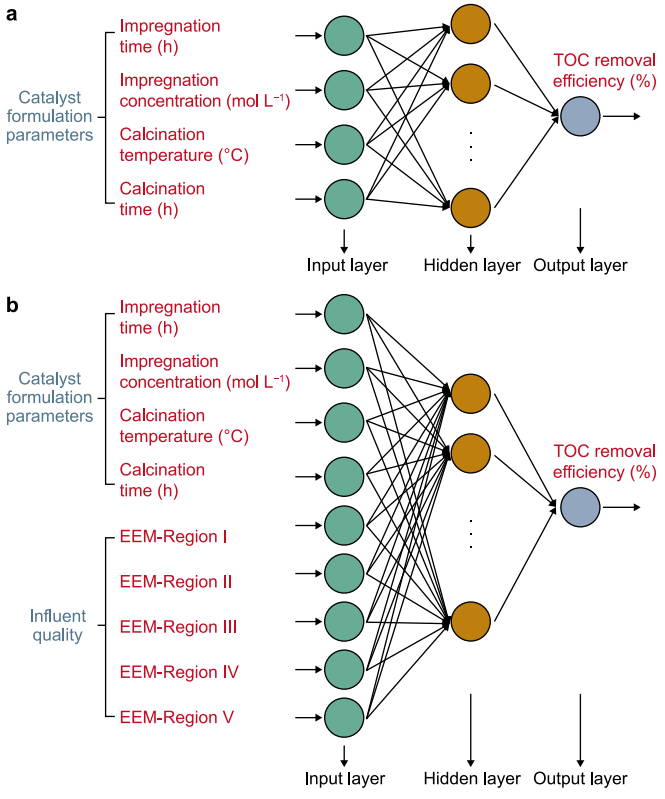

Fig. 1. Structures of ANN models: **a**, ANN_1; **b**, ANN_2.

3. Results and discussion

3.1. Selection input variables of ANN model

ANN modeling prediction is based on a functional relationship between the predicted and training values. If the training data have too many input variables that are weakly correlated with the predicted value, they will affect the generalization ability of the neural network and further reduce the prediction accuracy of the model [25]. Therefore, input variables were investigated to determine the significance of the considered indexes on the Mn/γ-Al_2O_3 catalyst performance. To explore the optimization of catalyst formulation based on wastewater quality characteristics, two layers of indexes were mainly considered when screening the input variables of the ANN model: (i) Catalyst formulation, including impregnation concentration, impregnation time, calcination temperature, and calcination time; and (ii) influent quality indexes, including COD, TOC, UV_{254}, and five fluorescence region intensities (regions I, II, III, IV, and V). The notability inspection was based on principal component analysis and equation (4), which represents the impact of each index on the output variable (details of principal component analysis results are provided in Text S5). Fig. 2 shows that the five fluorescence region intensities were the most important indexes among others, while TOC, COD, and UV_{254} made little contribution. This was mainly due to fluorescence data providing information on

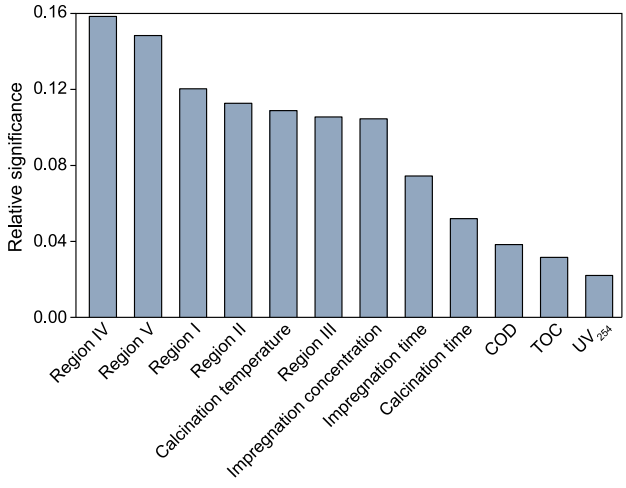

Fig. 2. Important contributions of indexes to output variable.

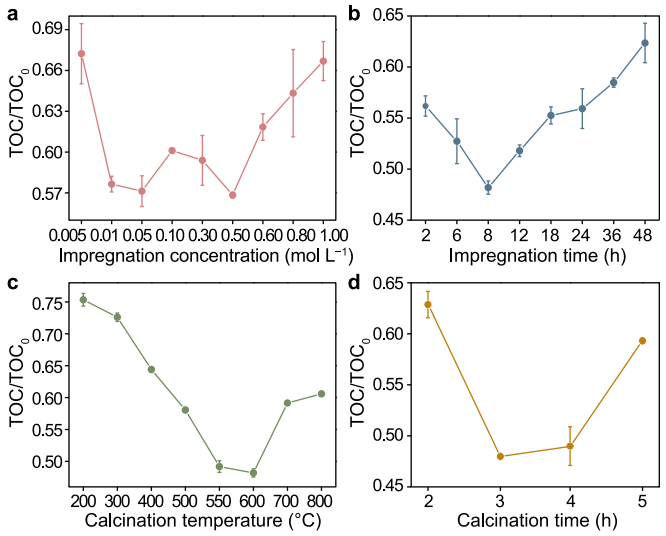

Fig. 3. Influence of catalyst formulation on TOC removal efficiency by the catalytic ozonation process: **a**, impregnation concentration; **b**, impregnation time; **c**, calcination temperature; **d**, calcination time. Conditions: pH 7–8; PSE: 1 L; [Mn/γ-Al_2O_3 catalyst]: 300 g L^{-1}; time: 60 min; [O_3]: 3 mg L^{-1}.

the composition and concentration of organics in the influent, which was inadequate for TOC, COD, and UV_{254} [18,19]. Furthermore, the relative significance of the four parameters of catalyst formulation was more than 0.05, indicating that the effect on the output variable was not negligible.

The results in Fig. 2 suggest that changes in fluorescent organics significantly influenced catalyst performance. Studies have reported a linear correlation between fluorescence intensity and COD or TOC [26,27]. Tyrosine-like components show strong correlations with COD ($R^2 = 0.83$) in wastewater treatment plants [26], while humic-like and fulvic-like acids are linearly correlated with TOC in urban lake water, with R^2 values of 0.97 and 0.99, respectively [27]. Fig. S3 shows that the R^2 values between the five fluorescence region intensities and TOC were in the range of 0.92–0.99, respectively, showing a strong positive correlation. Compared with regions I, II, III, and V, region IV showed the strongest linear relationship ($R^2 = 0.99$) with the TOC, showing that soluble microbial products were dominant contributors to organic carbon in the catalytic ozonation process. This result agreed with petrochemical wastewater containing large amounts of refractory toxic organics, and microbial products formed by hydrolysis acidification–anoxic/oxic process being discharged into the secondary sedimentation tank. This indicated that fluorescent organics could substitute for the comprehensive index of TOC in PSE, thus affecting catalyst performance.

Furthermore, catalyst activity is often reported to be closely related to catalyst formulation [28,29]. The impregnation concentration and time can lead to an uneven distribution of the active phase [28]. The effect of calcination temperature and time is mainly caused by the mass and heat transfer process, which affects the specific surface area and crystallinity of the catalyst [30]. Therefore, the effect of catalyst formulation on TOC removal efficiency using the Mn/γ-Al_2O_3 catalytic ozonation process was discussed. According to Fig. 3a and b, at an impregnation solution concentration above 0.5 mol L^{-1} and impregnation time longer than 8 h, TOC removal efficiency decreased from 43.16% to 51.82%, respectively. Excess concentration and time cause metal to cover the surface or block the pore structure of γ-Al_2O_3, reducing the number of catalytic sites [31,32]. As shown in Fig. 3c and d, TOC removal efficiency reached a maximum (52.02%) when roasted at 600 °C for 3 h. This excellent catalytic activity was due to Mn oxide crystals forming at 400–600 °C and uniformly distributing on the γ-Al_2O_3 surface [33]. Notably, with surplus calcination temperature and time, the catalyst crystal melted and the pore collapsed, which led to the decreased adsorbability of the catalyst surface toward organic matter [10,29].

Therefore, catalyst formulation (impregnation concentration, impregnation time, calcination temperature, and calcination time) and the five fluorescence region intensities (regions I, II, III, IV, and V) in the influent were selected as input variables for the ANN model.

3.2. ANN modeling and optimization

To confirm whether catalyst activity was closely related to the wastewater characteristics, two types of "feedforward neural network" model were developed (Fig. 1), and their prediction accuracy compared. The catalyst formulation parameters were selected as ANN_1 input variables, while catalyst formulation and the five fluorescence region intensities in the influent were simultaneously applied as ANN_2 input variables.

In ANN models, hidden neurons affect the establishment of models and result prediction accuracy. The number of hidden neurons not only concerns the number of nodes in the input and output layers, but also the types of conversion function and characteristics of the samples [34]. The RSME values of ANN_1 and ANN_2 as a function of the neuron number in the hidden layer are shown in Fig. 4a. In the ANN_1 curve, the curve oscillating increased with the number of hidden neurons between 15 and 50, and the RMSE had five relatively low values of 23, 24, 25, 36, and 38. Fig. 4b shows that the ANN_1 model fitting was optimal when the number of hidden neurons was 36, with RMSE and R^2 values of 6.47 and 0.4542, respectively. For ANN_2 models, the relatively low RMSE values were 23, 29, 30, and 34. The RMSE increased with an increasing number of neurons, illustrating the unexpected signal of overfitting. This was attributed to the complexity of the neural network structure leading to a long algorithm training time [15]. As shown in Fig. 4c, when the number of hidden neurons was 23, the fitting of the ANN_2 model was optimal, with RMSE and R^2 values of 3.06 and 0.79, respectively. Therefore, without affecting the model prediction, 36 and 23 neurons were selected as the hidden layer of ANN_1 and ANN_2, respectively.

The learning rate in the BP neural network represents the updating speed of the network weight and threshold value [24]. An

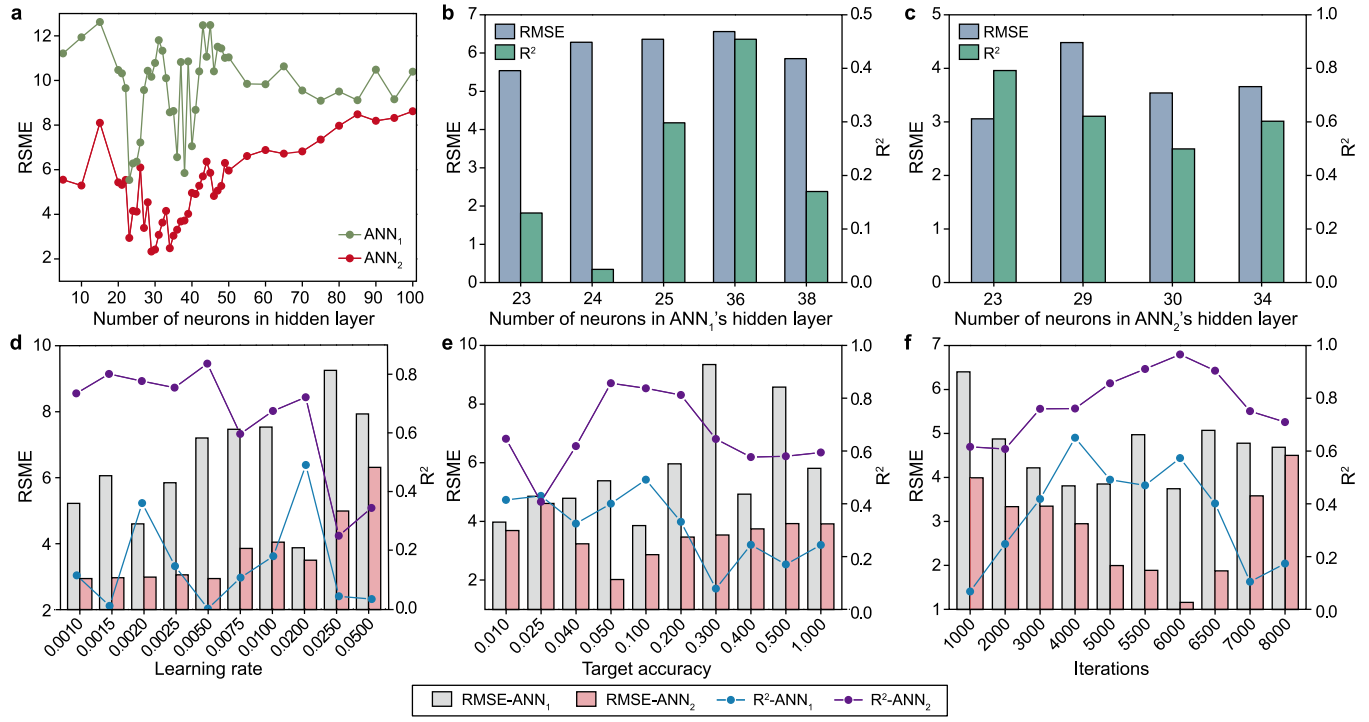

Fig. 4. Optimization of ANN_1 and ANN_2 model parameters. **a**, RMSE of ANN_1 and ANN_2 as a function of neuron number in the hidden layer. **b**, The number of neurons in the hidden layer with ANN_1. **c**, The number of neurons in the hidden layer with ANN_2. **d**, Learning rate. **e**, Target accuracy. **f**, Iterations.

excessive learning rate value will cause rapid updating of the range, resulting in declining prediction stability in the network. Meanwhile, an insufficient learning rate value will lead to a slow and inadequate network training speed [35]. Furthermore, setting target accuracy and iterations determines the stopping conditions of network training [34]. Therefore, the appropriate model operation parameters must be optimized to achieve the global minimum error possible in the network training. The optimization procedure needs to meet the requirements of network stability while ensuring prediction accuracy and running speed. Fig. 4d–f shows the optimization results for the operating parameters of the two models. The optimal parameters of the ANN_1 model were determined to be a learning rate of 0.02, a target accuracy of 0.1, 4000 iterations, and RSME and R^2 values of 3.83 and 0.6506, respectively. Meanwhile, the optimal parameters of the ANN_2 model were determined to be a learning rate of 0.005, a target accuracy of 0.05, 6000 iterations, and RMSE and R^2 values of 1.16 and 0.9659, respectively.

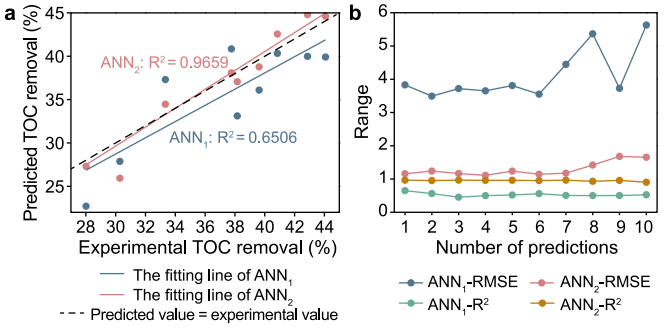

Fig. 5. Comparison of prediction accuracy and stability between ANN_1 and ANN_2 models. **a**, Fitting curve of predicted and experimental TOC removal efficiency. **b**, RMSE and R^2 values of ten consecutive predictions.

According to Fig. 5, the results of ten consecutive predictions showed that the RMSE and R^2 values of the ANN_1 prediction sample group fluctuated in the ranges of 3.49–5.63 and 0.4535–0.6506, respectively; while those of the ANN_2 prediction sample group fluctuated in the ranges of 1.11–1.68 and 0.9027–0.9659, respectively. The R^2 values of >0.9 demonstrated the robustness and good generalization of the ANN_2 model. The robustness of the ANN model in this study was consistent with previous reports. Karaman et al. [25] reported that an optimized ANN model predicted the adsorption behavior of anionic dyes on biomass-modified carbon materials with an R^2 value of 0.9996. Alsaffar et al. [15] accurately predicted the carbon deposition of catalysts through the training of an ANN model, with $R^2 = 0.987$ for the predicted and observed values. Suparmaniam et al. [36] reported that ANN achieved a high prediction accuracy for the microalgae flocculation process ($R^2 > 0.98$). Compared with ANN_1, ANN_2 showed higher accuracy and stability. Therefore, the interaction between catalyst formulation and influent quality could be considered to affect the ANN output. Therefore, the ANN_2 model was selected for subsequent catalyst optimization in this study.

3.3. Combining fluorescent spectroscopy and ANN model for catalyst formulation

In this study, fluorescence spectroscopy was applied for preliminary screening of the range of catalyst formulations, and then the optimized catalyst formulation was determined by ANN model verification. Pearson product-moment correlation coefficient was used to measure the correlation (linear correlation) between two variables X (catalyst formula) and Y (influent fluorescence intensity). The correlation strength, represented by the Pearson product-moment correlation coefficient, is shown in Table S7. As shown in Fig. 6, the Pearson product-moment correlation coefficients of impregnation concentration with fluorescent regions

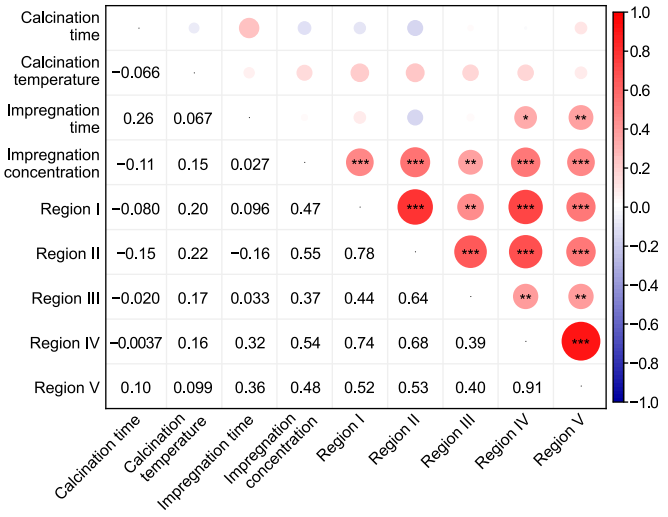

Fig. 6. Pearson relationship between TOC variation and ANN_2 model input variables. $*p \leq 0.05$; $**p \leq 0.01$; $***p \leq 0.001$.

I–V were in the range of 0.37–0.55. These results indicated a moderate positive correlation between the impregnation concentration and regions I, II, IV, and V. Furthermore, the impregnation time showed a weak positive correlation with regions IV and V, with correlation coefficients of 0.32 and 0.36, respectively. To further obtain the range of catalyst formulations using influent fluorescence information, contour diagrams were used to visualize the interaction between the catalyst formulation (impregnation concentration and impregnation time) and fluorescent organics.

Fig. 7a shows the effect of impregnation concentration and influent fluorescent organics on the catalyst performance. TOC removal efficiency increased with increasing impregnation concentration in regions I, IV, and V at low fluorescence intensity. Furthermore, when the impregnation concentration of $Mn(NO_3)_2$ was less than 0.3 mol L^{-1}, TOC removal efficiencies in regions I, IV, and V remained above 30%, with TOC removal efficiencies in regions II and III being more than 41.79%, exhibiting excellent catalytic performance. This was consistent with the conclusions of previous studies. For example, Luo et al. [31] deemed that an insufficient impregnation solution concentration caused low catalyst activity, while Tong et al. [32] reported that the pore structure of Fe-SBA-16 was destroyed because of the over-doping of Fe. Therefore, when influent fluorescent organics are dominated by regions II and III, the $Mn(NO_3)_2$ concentration should be < 0.3 mol L^{-1}.

As shown in Fig. 7b, for region IV, the peak values of TOC removal, represented by the red color in the plot, were obtained within an impregnation time of 10 h. This means that the rapid reaction between the active component and catalyst surface is conducive to promoting the decomposition of O_3 into •OH, which effectively mineralizes organics [37]. TOC removal efficiency increased in region V with an extended impregnation time, and remained over 40% with an impregnation time of >30 h. This was mainly due to diffusion in the porous structure of the Mn/Al_2O_3 catalyst being the main factor enhancing catalyst performance. Therefore, if the influent fluorescent organic matter is dominated by region V, an impregnation time of over 30 h should be selected, but the adsorption balance and dissolution rate of metal ions on the carrier should be considered. Meanwhile, an impregnation time of less than 10 h was advantageous to the treatment of influent fluorescent organic matter dominated by region IV.

Using PSE as an example, the range of catalyst formulations could be obtained by analyzing the fluorescence characteristics. Fig. S5 shows the contents II of fluorescent organics in PSE, which were in the order of region II > V > IV > III > I, with the average proportions of region II and IV in PSE being 33.26% and 28.94%, respectively. This confirmed that PSE was dominated by tryptophan-like aromatic proteins and soluble microbial

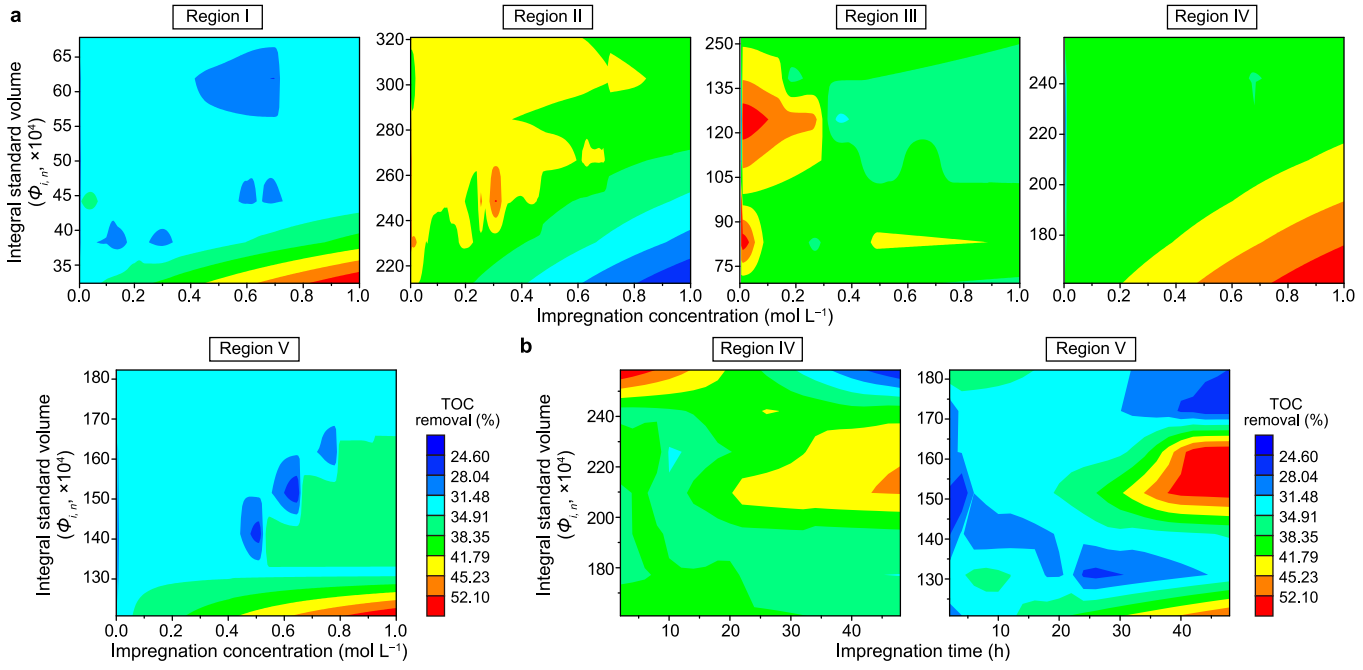

Fig. 7. Interaction of catalyst formulation and influent quality on catalyst performance (TOC removal efficiency). **a**, Impregnation concentration and fluorescent organics. **b**, Impregnation time and fluorescent organics.

metabolites. The results for fluorescence characteristics in PSE agreed with Fu et al. [22]. Therefore, Mn/γ-Al_2O_3 catalyst was optimized by the ANN_2 model based on an impregnation concentration and time of less than 0.3 mol L^{-1} and 10 h, respectively.

The range of catalyst formulation mentioned above was selected as the boundary of the ANN_2 model. The boundary ranges were a $Mn(NO_3)_2$ impregnation concentration of 0.01–0.3 mol L^{-1}, an impregnation time of 4–10 h, a calcination temperature of 300–600 °C, and a calcination time of 2–4 h. The trained ANN_2 model was then used to obtain the optimum catalyst formulation using an enumeration algorithm. The optimal Mn/γ-Al_2O_3 formulation was as follows: 0.155 mol L^{-1} of [$Mn(NO_3)_2$] for 8.5 h, and a calcination temperature of 600 °C for 3.5 h. The ANN-predicted and experimental values for TOC removal for the optimal Mn/γ-Al_2O_3 catalyst were 54.48% and 53.96%, respectively. To confirm the correctness of the ANN model, testing was conducted using 15 groups. Fig. S6 and Table S8 show that the ANN-predicted and experimental R^2 value was 0.9593, indicating that the developed ANN model agreed well with Mn/γ-Al_2O_3 catalyst performance. Therefore, the ANN model combined with fluorescence spectroscopy could be an effective method for optimizing ozonation catalyst formulation.

3.4. Characterization of optimal catalyst

Characterization of the catalyst with the highest TOC removal efficiency predicted by the ANN model was conducted to confirm catalyst performance. From the SEM images (Fig. 8a and b), compared with the γ-Al_2O_3 carrier, the Mn/γ-Al_2O_3 catalyst showed a uniform rough elliptic particle structure and a dense layered pore structure on the catalyst surface, which formed during calcination of the catalyst [38,39]. The SEM-EDS results (Fig. S7 and Table S9) showed that the weight percentage of Mn was 0.87%, indicating that the metal oxide was successfully loaded into the carrier. The specific surface area and pore size distribution of the samples were observed using N_2 adsorption–desorption isotherms (Fig. 8 and Table S10). γ-Al_2O_3 and Mn/γ-Al_2O_3 both exhibited an H_3-type hysteresis loop in the desorption branch when P/P_0 was 0.45 and 0.55, respectively, belonging to a type-IV(a) isothermal curve [40]. These results suggested that γ-Al_2O_3 and Mn/γ-Al_2O_3 were typical mesoporous structures. Compared with that of γ-Al_2O_3, the S_{BET} value of Mn/γ-Al_2O_3 had decreased by 23.76%, and the average diameter and pore volume had increased by 31.49% and 11.66%, respectively, which was consistent with the pore size distribution results shown in the right of Fig. 8c and d. This was attributed to γ-Al_2O_3 being the main contributor to S_{BET}, and high-temperature roasting, resulting in the collapse of micropores to form mesoporous and macroporous structures, which was conducive to the dispersion of Mn oxide [11].

XRD measurements were used to elucidate changes in the crystal structure between the γ-Al_2O_3 carrier and Mn/γ-Al_2O_3 catalyst, with the results shown in Fig. 9a. For the γ-Al_2O_3 carrier, three diffraction peaks were observed at 19.42°, 37.60°, 45.86°, and 67.03°, corresponding to the Al_2O_3 crystal structure (JCPDS

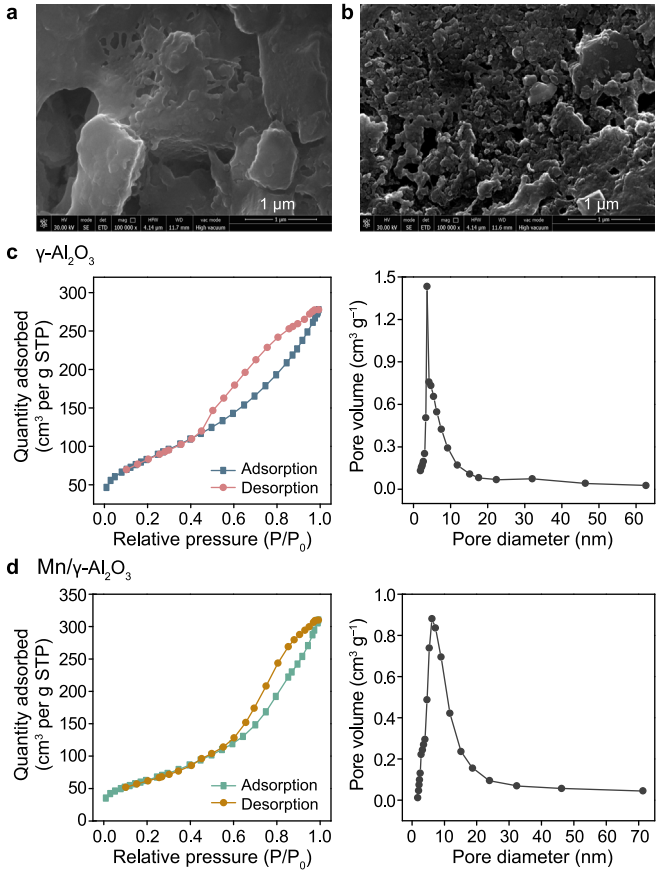

Fig. 8. **a**–**b**, SEM images of γ-Al_2O_3 (**a**) and Mn/γ-Al_2O_3 (**b**). **c**–**d**, Adsorption-desorption isotherms (left) and pore size distributions (right) of γ-Al_2O_3 (**c**) and Mn/γ-Al_2O_3 (**d**).

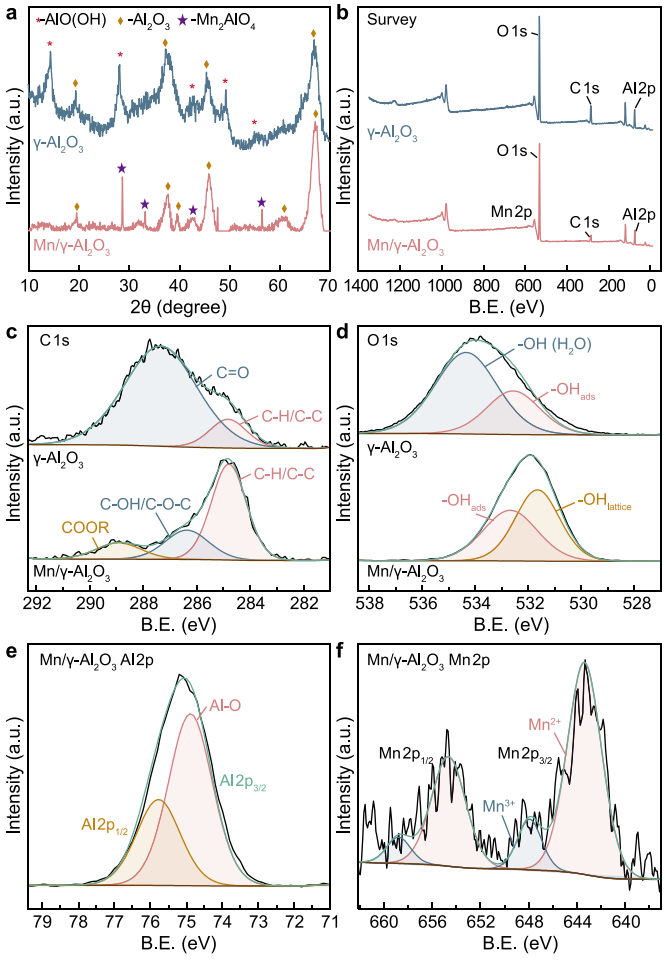

Fig. 9. **a**, XRD spectra of γ-Al_2O_3 and Mn/γ-Al_2O_3. **b**, Survey XPS spectra. **c**, Fitted spectra of C1s. **d**, Fitted spectra of O1s. **e**, Fitted spectra of Al 2p. **f**, Fitted spectra of Mn 2p.

10–0425). The XRD patterns showed that AlO(OH) in the γ-Al_2O_3 carrier belonged to the rhombic system (JCPDS 88–2112), while the Mn/γ-Al_2O_3 catalyst did not, mainly owing to the diffraction peak of AlO(OH) disappearing when the calcination temperature of γ-Al_2O_3 was above 450 °C [41]. Four diffraction peaks were observed for the Mn/γ-Al_2O_3 catalyst, at 28.79°, 33.524°, 43.188°, and 57.128°, belonging to the (220), (311), (400), and (511) planes, respectively, which matched the cubic spinel phase of Mn_2AlO_4 (JCPDS 29–0881) [42]. Studies have shown the existence of ion leaching by manganese oxides. However, bonding between Mn and Al can effectively maintain structural stability in the catalytic ozonation process, reducing Mn ion leaching [43].

Catalyst activity is affected by the metal composition and chemical valence state of the catalyst. Therefore, γ-Al_2O_3 and Mn/γ-Al_2O_3 were analyzed by XPS (Fig. 9b–f). The survey XPS spectra (Fig. 9b) showed that all elements (C, O, and Al) in the γ-Al_2O_3 carrier and Mn were present in the synthesized Mn/γ-Al_2O_3 catalyst. The fitted spectrum of C 1s (Fig. 9c) in γ-Al_2O_3 exhibited a C–H/C–C peak at 284.80 eV and a C=O peak at 287.33 eV, while Mn/γ-Al_2O_3 could be divided into three main peaks, at 284.80, 286.36, and 288.92 eV, corresponding to C–H/C–C, C–OH, and O–C=O, respectively. The C–OH and C=O structures acted as catalytic sites for the rapid decomposition of O_3 to •OH [44]. The fitted spectra of O 1s (Fig. 9c) showed two peaks, namely, for adsorbed OH at 532.67 eV and lattice OH at 531.65 eV, which were attributed to the metal oxide loaded onto the γ-Al_2O_3 carrier occupying the surface hydroxyl position and forming the oxygen structure of the metal oxide lattice [45]. Furthermore, ATR-FTIR spectroscopy (Fig. S8) showed that O–H and C=O were the main surface functional groups of Mn/γ-Al_2O_3, which agreed with the XPS results. For the Mn/γ-Al_2O_3 catalyst, the two characteristic peaks of Al $2p_{3/2}$ (74.89 eV) and Al $2p_{1/2}$ (75.78 eV) in the fitted Al 2p spectrum (Fig. 9e) were Al–OH on the γ-Al_2O_3 surface, which could act as the catalytic site [46]. The fitted Mn 2p spectrum, exhibiting two spin-orbit doublets of Mn $2p_{3/2}$ and Mn $2p_{1/2}$, is shown in Fig. 9f. The binding energy peaks of Mn/γ-Al_2O_3 located at 643.36 and 654.66 eV confirmed the presence of Mn^{2+}, while the other two peaks at 647.91 and 658.81 eV were attributed to Mn^{3+} [47]. The presence of Mn^{2+}/Mn^{3+} redox electron pairs on the surface of Mn/γ-Al_2O_3 suggested that Mn/γ-Al_2O_3 could catalyze the production of reactive oxygen species (ROS) from O_3 [8].

3.5. Catalytic performance and catalytic mechanism of optimal catalyst

The catalytic performance of the optimized Mn/γ-Al_2O_3 was evaluated and compared with that of the single ozonation and adsorption systems. Fig. S9 shows that the TOC removal efficiencies of the adsorption, single ozonation, and catalytic ozonation systems were 9.86%, 15.19%, and 53.52%, respectively. The TOC removal efficiencies of adsorption and single ozonation systems accounted for 18.96% and 29.20% of the Mn/γ-Al_2O_3 catalytic ozonation system, respectively. The above results indicated that the Mn/γ-Al_2O_3 catalytic ozonation system involved the synergistic effects of oxidation (•OH and O_3 molecules) and the Mn/γ-Al_2O_3 catalyst. The Mn component in the Mn/Al_2O_3 catalyst was conducive to the adsorption of water molecules to form surface hydroxyl groups, which further promoted the decomposition of O_3 into •OH, enhancing the mineralization of organics [48,49]. Furthermore, in the optimized Mn/γ-Al_2O_3 catalytic ozonation system, the reaction kinetics matched the pseudo-second-order kinetics with a R^2 value of 0.9786, as shown in Table S11. Fig. S10 shows that the carbon oxidation state [50] increased from 1.47 to 1.87, reflecting significant mineralization, meaning that the catalytic ozonation process transformed refractory organics into biodegradable substances.

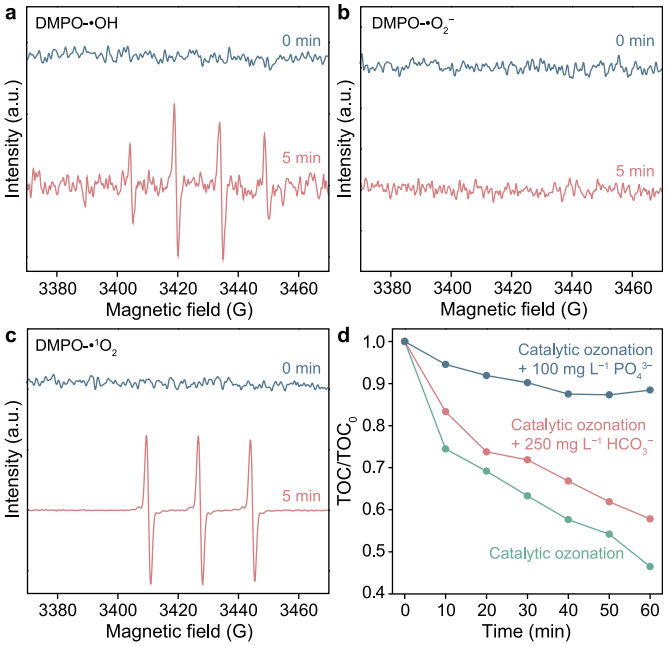

Fig. 10. **a**–**c**, ESR spectra of different ROS in the Mn/γ-Al_2O_3 catalytic ozonation system: •OH (**a**); $•O_2^-$ (**b**); $^1O_2$ (**c**). **d**, The effect of ions HCO_3^- and PO_4^{3-} on the Mn/γ-Al_2O_3 catalytic ozonation system.

Ten cycling tests were conducted for the Mn/γ-Al_2O_3 catalyst optimized by the ANN model (Table S12). The TOC removal efficiency of the optimized Mn/γ-Al_2O_3 in the tenth cycle was 41.74%, which had only decreased by 6.24% compared with that in the first cycle, indicating the excellent reusability and stability of Mn/γ-Al_2O_3. The O_3 utilization rate of the single catalyst cycle test was approximately 90%, suggesting high O_3 utilization in the Mn/γ-Al_2O_3 catalytic ozonation system. Furthermore, the maximum dissolution concentration of Al ions was 70 μg L^{-1}, which was attributed to Al^{3+} release from the hydrolysis of Al_2O_3 on the catalyst surface. A low leaching concentration of Al^{3+} indicated that the γ-Al_2O_3 carrier was stable and did not reduce catalyst activity. Meanwhile, the average COD and TOC of the effluent reached 30.2 and 9.73 mg L^{-1}, respectively, with the effluent meeting the Emission Standard of Pollutants for the Petroleum Chemistry Industry (GB 31571-2015, China).

To investigate the main ROS in the Mn/γ-Al_2O_3 catalytic ozonation system, electron spin resonance (ESR) analysis was performed. As shown in Fig. 10a and c, DMPO-•OH characteristic peaks with an intensity ratio of 1:2:2:1 and TEMP-$^1O_2$ characteristic peaks with an intensity ratio of 1:1:1 appeared in the Mn/γ-Al_2O_3 catalytic ozonation system. However, as shown in Fig. 10b, no obvious DMPO-$•O_2^-$ signal peaks were detected. The above results indicated that the main reason for improved catalytic performance in the Mn/γ-Al_2O_3 catalytic ozonation system was that Mn/γ-Al_2O_3 was conducive to radical (•OH) and non-radical ($^1O_2$) generation.

The composition of wastewater is complex, and anions in wastewater can affect catalyst activity. As shown in Fig. 10d, the effects of carbonate ions (HCO_3^-) and phosphate ions (PO_4^{3-}) on the Mn/γ-Al_2O_3 catalytic ozonation system were investigated. TOC removal efficiency decreased from 52.02% to 42.18% with 250 mg L^{-1} HCO_3^-, indicating that HCO_3^- quenched •OH in the system. In contrast, phosphate can be adsorbed on the catalyst surface and effectively replace surface hydroxyl groups. The presence of 100 mg L^{-1} PO_4^{3-} significantly inhibited the mineralization of organics, and TOC removal decreased to 11.55%. This result

proved that surface hydroxyl groups were the active catalytic sites. Therefore, the following catalytic mechanism was proposed using our results (equations (5)–(10)):

$$Mn^{2+} + O_3 + H^+ \rightarrow Mn^{3+} + \bullet OH + O_2 \quad (5)$$

$$O_3 + \bullet OH \rightarrow O_2 + HO_2^- \bullet \quad (6)$$

$$Mn^{3+} + HO_2^- \bullet + OH^- \rightarrow Mn^{2+} + H_2O + O_2 \quad (7)$$

$$Mn^{2+} \bullet OH \rightarrow Mn^{3+} + OH^- \quad (8)$$

$$\bullet OH + HCO_3^- \rightarrow OH^- + HCO_3 \bullet \quad (9)$$

$$\bullet OH / O_3 + \text{organics} \rightarrow CO_2 + H_2O \quad (10)$$

4. Conclusions

In summary, the ANN algorithm in machine learning combined with fluorescence spectroscopy successfully optimized catalyst formulation for PSE treatment using the catalytic ozonation process.

The input variables of the ANN model were determined, including catalyst formulation (impregnation concentration, impregnation time, calcination temperature, and calcination time) and influent fluorescence region intensity (regions I, II, III, IV, and V). The RMSE and R^2 values of TOC removal between experimental values and those predicted by the ANN model were 1.16 and 0.9659, respectively.

Visualization of the fluorescence spectroscopy allowed preliminary screening of the range of catalyst formulation. The results showed that the impregnation concentration of $Mn(NO_3)_2$ was less than 0.3 mol L^{-1} when influent fluorescent organics were dominated by regions II and III. Furthermore, an impregnation time of over 30 h was optimal when dominated by region V, while an impregnation time shorter than 10 h was optimal when dominated by region IV.

The optimal formulation of Mn/γ-Al_2O_3 obtained from the trained ANN model was impregnation with 0.155 mol L^{-1} $Mn(NO_3)_2$ for 8.5 h and calcination at 600 °C for 3.5 h. The predicted and experimental TOC removal efficiencies of the optimal Mn/γ-Al_2O_3 catalyst were 54.48% and 53.96%, respectively. ESR analysis indicated that •OH and $^1O_2$ were involved in the Mn/γ-Al_2O_3 catalytic reaction. Specifically, surface hydroxyl groups were the main catalytic sites for •OH generation.

This work provides an approach to the rapid design and optimization of ozonation catalysts for various types of industrial wastewater using machine learning combined with fluorescence spectroscopy.

CRediT authorship contribution statement

Min Li: Conceptualization, Methodology, Experiments, Data Curation, Writing - Original draft preparation. **Liya Fu:** Discussion and analysis, Writing - Reviewing and Editing. **Liyan Deng:** Investigation. **Yingming Hu:** Data Curation. **Yue Yuan:** Writing - Reviewing and Editing. **Changyong Wu:** Discussion and analysis, Writing- Reviewing and Editing.

Declaration of competing interest

The authors declare that they have no known competing financial interests or personal relationships that could have appeared to influence the work reported in this manuscript.

Acknowledgments

This work was financially supported by the Fundamental Research Funds for the Central Public-interest Scientific Institution 2022YSKY-70 and the National Key R&D Program of China (No. 2020YFC1806302).

Appendix A. Supplementary data

Supplementary data to this article can be found online at https://doi.org/10.1016/j.ese.2023.100244.

References

[1] X. Tian, Y. Song, Z. Shen, Y. Zhou, K. Wang, X. Jin, Z. Han, T. Liu, A comprehensive review on toxic petrochemical wastewater pretreatment and advanced treatment, J. Clean. Prod. 245 (2020), 118692, https://doi.org/10.1016/j.jclepro.2019.118692.

[2] M. Gągol, A. Przyjazny, G. Boczkaj, Wastewater treatment by means of advanced oxidation processes based on cavitation – a review, Chem. Eng. J. 338 (2018) 599–627, https://doi.org/10.1016/j.cej.2018.01.049.

[3] M. Moradi, B. Kakavandi, A. Bahadoran, S. Giannakis, E. Dehghanifard, Intensification of persulfate-mediated elimination of bisphenol A by a spinel cobalt ferrite-anchored g-C_3N_4 S-scheme photocatalyst: catalytic synergies and mechanistic interpretation, Separ. Purif. Technol. 285 (2022), 120313, https://doi.org/10.1016/j.seppur.2021.120313.

[4] Y. Lee, M. Cui, J. Choi, Y. Jeong, J. Khim, Demonstration and evaluation of potential configuration options for shale-wastewater treatment plant by combining several unit processes, J. Clean. Prod. 232 (2019) 867–876, https://doi.org/10.1016/j.jclepro.2019.05.381.

[5] Z.Q. Liu, C. Huang, J.Y. Li, J. Yang, B. Qu, S.Q. Yang, Y.H. Cui, Y. Yan, S. Sun, X. Wu, Activated carbon catalytic ozonation of reverse osmosis concentrate after coagulation pretreatment from coal gasification wastewater reclamation for zero liquid discharge, J. Clean. Prod. 286 (2021), 124951, https://doi.org/10.1016/j.jclepro.2020.124951.

[6] C.V. Rekhate, J.K. Srivastava, Recent advances in ozone-based advanced oxidation processes for treatment of wastewater- A review, CEJ Adv. 3 (2020), 100031, https://doi.org/10.1016/j.ceja.2020.100031.

[7] J. Wang, Z. Bai, Fe-based catalysts for heterogeneous catalytic ozonation of emerging contaminants in water and wastewater, Chem. Eng. J. 312 (2017) 79–98, https://doi.org/10.1016/j.cej.2016.11.118.

[8] F. Nawaz, H. Cao, Y. Xie, J. Xiao, Y. Chen, Z.A. Ghazi, Selection of active phase of MnO_2 for catalytic ozonation of 4-nitrophenol, Chemosphere 168 (2017) 1457–1466, https://doi.org/10.1016/j.chemosphere.2016.11.138.

[9] F. Nawaz, Y. Xie, J. Xiao, H. Cao, Z.A. Ghazi, Z. Guo, Y. Chen, The influence of the substituent on the phenol oxidation rate and reactive species in cubic MnO_2 catalytic ozonation, Catal. Sci. Technol. 6 (21) (2016) 7875–7884, https://doi.org/10.1039/c6cy01542e.

[10] J. Wang, X. Quan, S. Chen, H. Yu, G. Liu, Enhanced catalytic ozonation by highly dispersed CeO2 on carbon nanotubes for mineralization of organic pollutants, J. Hazard Mater. 368 (2019) 621–629, https://doi.org/10.1016/j.jhazmat.2019.01.095.

[11] Y. Wang, W. Yang, X. Yin, Y. Liu, The role of Mn-doping for catalytic ozonation of phenol using Mn/γ-Al_2O_3 nanocatalyst: performance and mechanism, J. Environ. Chem. Eng. 4 (3) (2016) 3415–3425, https://doi.org/10.1016/j.jece.2016.07.016.

[12] B. Burger, P.M. Maffettone, V.V. Gusev, C.M. Aitchison, Y. Bai, X. Wang, X. Li, B.M. Alston, B. Li, R. Clowes, N. Rankin, B. Harris, R.S. Sprick, A.I. Cooper, A mobile robotic chemist, Nature 583 (7815) (2020) 237–241, https://doi.org/10.1038/s41586-020-2442-2.

[13] H.A. Garona, F.M. Cavalcanti, T.F. de Abreu, M. Schmal, R.M.B. Alves, Evaluation of Fischer-Tropsch synthesis to light olefins over Co- and Fe-based catalysts using artificial neural network, J. Clean. Prod. 321 (2021), https://doi.org/10.1016/j.jclepro.2021.129003.

[14] H. Jafarzadeh, C. Karaman, A. Güngör, O. Karaman, P.-L. Show, P. Sami, A.A. Mehrizi, Hydrogen production via sodium borohydride hydrolysis catalyzed by cobalt ferrite anchored nitrogen-and sulfur co-doped graphene hybrid nanocatalyst: artificial neural network modeling approach, Chem. Eng. Res. Des. 183 (2022) 557–566, https://doi.org/10.1016/j.cherd.2022.05.038.

[15] M.A. Alsaffar, B.V. Ayodele, S.I. Mustapa, Scavenging carbon deposition on alumina supported cobalt catalyst during renewable hydrogen-rich syngas production by methane dry reforming using artificial intelligence modeling technique, J. Clean. Prod. 247 (2020), https://doi.org/10.1016/j.jclepro.2019.119168.

[16] K. Lu, H. Gao, H. Yu, D. Liu, N. Zhu, K. Wan, Insight into variations of DOM fractions in different latitudinal rural black-odor waterbodies of eastern China using fluorescence spectroscopy coupled with structure equation model, Sci.

Total Environ. 816 (2022), 151531, https://doi.org/10.1016/j.scitotenv.2021.151531.
[17] C.L. Osburn, L.T. Handsel, M.P. Mikan, H.W. Paerl, M.T. Montgomery, Fluorescence tracking of dissolved and particulate organic matter quality in a river-dominated estuary, Environ. Sci. Technol. 46 (16) (2012) 8628–8636, https://doi.org/10.1021/es3007723.
[18] W. Shi, W.E. Zhuang, J. Hur, L. Yang, Monitoring dissolved organic matter in wastewater and drinking water treatments using spectroscopic analysis and ultra-high resolution mass spectrometry, Water Res. 188 (2021), 116406, https://doi.org/10.1016/j.watres.2020.116406.
[19] M.J.M. Wells, J. Hooper, G.A. Mullins, K.Y. Bell, Development of a fluorescence EEM-PARAFAC model for potable water reuse monitoring: implications for inter-component protein-fulvic-humic interactions, Sci. Total Environ. 820 (2022), 153070, https://doi.org/10.1016/j.scitotenv.2022.153070.
[20] M. Heibati, C.A. Stedmon, K. Stenroth, S. Rauch, J. Toljander, M. Save-Soderbergh, K.R. Murphy, Assessment of drinking water quality at the tap using fluorescence spectroscopy, Water Res. 125 (2017) 1–10, https://doi.org/10.1016/j.watres.2017.08.020.
[21] C. Wu, Y. Li, Y. Zhou, Z. Li, S. Zhang, H. Liu, Upgrading the Chinese biggest petrochemical wastewater treatment plant: technologies research and full scale application, Sci. Total Environ. 633 (2018) 189–197, https://doi.org/10.1016/j.scitotenv.2018.03.164.
[22] L.Y. Fu, C.Y. Wu, Y.X. Zhou, J.E. Zuo, G. Song, Y. Tan, Ozonation reactivity characteristics of dissolved organic matter in secondary petrochemical wastewater by single ozone, ozone/H_2O_2, and ozone/catalyst, Chemosphere 233 (2019) 34–43, https://doi.org/10.1016/j.chemosphere.2019.05.207.
[23] Y.C. Du, A. Stephanus, Levenberg-Marquardt neural network algorithm for degree of arteriovenous fistula stenosis classification using a dual optical photoplethysmography sensor, Sensors 18 (7) (2018), https://doi.org/10.3390/s18072322.
[24] D. Onalo, S. Adedigba, F. Khan, L.A. James, S. Butt, Data driven model for sonic well log prediction, J. Pet. Sci. Eng. 170 (2018) 1022–1037, https://doi.org/10.1016/j.petrol.2018.06.072.
[25] C. Karaman, O. Karaman, P.L. Show, H. Karimi-Maleh, N. Zare, Congo red dye removal from aqueous environment by cationic surfactant modified-biomass derived carbon: equilibrium, kinetic, and thermodynamic modeling, and forecasting via artificial neural network approach, Chemosphere 290 (2022), 133346, https://doi.org/10.1016/j.chemosphere.2021.133346.
[26] A. Goffin, S. Guerin-Rechdaoui, V. Rocher, G. Varrault, An environmentally friendly surrogate method for measuring the soluble chemical oxygen demand in wastewater: use of three-dimensional excitation and emission matrix fluorescence spectroscopy in wastewater treatment monitoring, Environ. Monit. Assess. 191 (7) (2019) 421, https://doi.org/10.1007/s10661-019-7570-5.
[27] R. Liu, J.R. Lead, A. Baker, Fluorescence characterization of cross flow ultrafiltration derived freshwater colloidal and dissolved organic matter, Chemosphere 68 (7) (2007) 1304–1311, https://doi.org/10.1016/j.chemosphere.2007.01.048.
[28] Y. Zhou, H. Zhang, Y. Yan, Catalytic oxidation of ethyl acetate over CuO/ZSM-5 catalysts: effect of preparation method, J. Taiwan Inst. Chem. E 84 (2018) 162–172, https://doi.org/10.1016/j.jtice.2018.01.016.
[29] Z. Zhu, G. Lu, Z. Zhang, Y. Guo, Y. Guo, Y. Wang, Highly active and stable Co_3O_4/ZSM-5 catalyst for propane oxidation: effect of the preparation method, ACS Catal. 3 (6) (2013) 1154–1164, https://doi.org/10.1021/cs400068v.
[30] Y. Wang, L. Chen, H. Cao, Z. Chi, C. Chen, X. Duan, Y. Xie, F. Qi, W. Song, J. Liu, S. Wang, Role of oxygen vacancies and Mn sites in hierarchical Mn_2O_3/$LaMnO_3$-δ perovskite composites for aqueous organic pollutants decontamination, Appl. Catal., B 245 (2019) 546–554, https://doi.org/10.1016/j.apcatb.2019.01.025.
[31] L. Luo, D. Zou, D. Lu, F. Yu, B. Xin, J. Ma, Study of catalytic ozonation for tetracycline hydrochloride degradation in water by silicate ore supported Co_3O_4, RSC Adv. 8 (72) (2018) 41109–41116, https://doi.org/10.1039/c8ra08402e.
[32] X. Tong, Z. Li, W. Chen, J. Wang, X. Li, J. Mu, Y. Tang, L. Li, Efficient catalytic ozonation of diclofenac by three-dimensional iron (Fe)-doped SBA-16 mesoporous structures, J. Colloid Interface Sci. 578 (2020) 461–470, https://doi.org/10.1016/j.jcis.2020.06.003.
[33] H. Wang, Y. Lu, Y. Han, C. Lu, H. Wan, Z. Xu, S. Zheng, Enhanced catalytic toluene oxidation by interaction between copper oxide and manganese oxide in Cu-O-Mn/γ-Al_2O_3 catalysts, Appl. Surf. Sci. 420 (2017) 260–266, https://doi.org/10.1016/j.apsusc.2017.05.133.
[34] E.-N. Dragoi, Y. Vasseghian, Modeling of mass transfer in vacuum membrane distillation process for radioactive wastewater treatment using artificial neural networks, Toxin Rev. 40 (4) (2020) 1526–1535, https://doi.org/10.1080/15569543.2020.1744659.
[35] W. Gao, A. Aslam, F. Li, Effect of equivalence ratio on gas distribution and performance parameters in air-gasification of asphaltene: a model based on Artificial Neural Network (ANN), Petrol. Sci. Technol. 37 (2) (2018) 202–207, https://doi.org/10.1080/10916466.2018.1533864.
[36] U. Suparmaniam, N.B. Shaik, M.K. Lam, J.W. Lim, Y. Uemura, S.H. Shuit, P.L. Show, I.S. Tan, K.T. Lee, Valorization of fish bone waste as novel bioflocculant for rapid microalgae harvesting: experimental evaluation and modelling using back propagation artificial neural network, J. Water Proc. Eng. 47 (2022), https://doi.org/10.1016/j.jwpe.2022.102808.
[37] S. Zhou, S. Zhu, Y. Shao, N. Gao, Characteristics of C-, N-DBPs formation from algal organic matter: role of molecular weight fractions and impacts of pre-ozonation, Water Res. 72 (2015) 381–390, https://doi.org/10.1016/j.watres.2014.11.023.
[38] Q. Dai, Z. Zhang, T. Zhan, Z.T. Hu, J. Chen, Catalytic ozonation for the degradation of 5-sulfosalicylic acid with spinel-type $ZnAl_2O_4$ prepared by hydrothermal, sol-gel, and coprecipitation methods: a comparison study, ACS Omega 3 (6) (2018) 6506–6512, https://doi.org/10.1021/acsomega.8b00263.
[39] L. Yang, M. Sheng, Y. Li, W. Xue, K. Li, G. Cao, A hybrid process of Fe-based catalytic ozonation and biodegradation for the treatment of industrial wastewater reverse osmosis concentrate, Chemosphere 238 (2020), 124639, https://doi.org/10.1016/j.chemosphere.2019.124639.
[40] M. Thommes, K. Kaneko, A.V. Neimark, J.P. Olivier, F. Rodriguez-Reinoso, J. Rouquerol, K.S.W. Sing, Physisorption of gases, with special reference to the evaluation of surface area and pore size distribution (IUPAC Technical Report), Pure Appl. Chem. 87 (9–10) (2015) 1051–1069, https://doi.org/10.1515/pac-2014-1117.
[41] Y. Li, J. Xu, M. Qian, J. Yu, J. Pan, B. Guan, The role of surface hydroxyl concentration on calcinated alumina in catalytic ozonation, Environ. Sci. Pollut. Res. Int. 26 (15) (2019) 15373–15380, https://doi.org/10.1007/s11356-019-04909-5.
[42] J.M. Munro, K. Latimer, M.K. Horton, S. Dwaraknath, K.A. Persson, An improved symmetry-based approach to reciprocal space path selection in band structure calculations, NPJ Comput. Mater. 6 (1) (2020), https://doi.org/10.1038/s41524-020-00383-7.
[43] C. Li, X. Han, F. Cheng, Y. Hu, C. Chen, J. Chen, Phase and composition controllable synthesis of cobalt manganese spinel nanoparticles towards efficient oxygen electrocatalysis, Nat. Commun. 6 (2015) 7345, https://doi.org/10.1038/ncomms8345.
[44] T. Chen, W. Gu, G. Li, Q. Wang, P. Liang, X. Zhang, X. Huang, Significant enhancement in catalytic ozonation efficacy: from granular to super-fine powdered activated carbon, Front. Environ. Sci. Eng. 12 (1) (2017), https://doi.org/10.1007/s11783-018-1022-2.
[45] P. Yan, J. Shen, Y. Zhou, L. Yuan, J. Kang, S. Wang, Z. Chen, Interface mechanism of catalytic ozonation in an α-$Fe_{0.9}Mn_{0.1}OOH$ aqueous suspension for the removal of iohexol, Appl. Catal., B 277 (2020), https://doi.org/10.1016/j.apcatb.2020.119055.
[46] B. Ealet, M.H. Elyakhloufi, E. Gillet, M. Ricci, Electronic and crystallographic structure of γ-alumina thin films, Thin Solid Films 250 (1) (1994) 92–100, https://doi.org/10.1016/0040-6090(94)90171-6.
[47] G. Rekha, R. Tholkappiyan, K. Vishista, F. Hamed, Systematic study on surface and magnetostructural changes in Mn-substituted dysprosium ferrite by hydrothermal method, Appl. Surf. Sci. 385 (2016) 171–181, https://doi.org/10.1016/j.apsusc.2016.05.092.
[48] S. Moradi, A.A. Isari, F. Hayati, R. Rezaei Kalantary, B. Kakavandi, Co-implanting of TiO_2 and liquid-phase-delaminated g-C_3N_4 on multi-functional graphene nanobridges for enhancing photocatalytic degradation of acetaminophen, Chem. Eng. J. 414 (2021), https://doi.org/10.1016/j.cej.2021.128618.
[49] S. Zhang, X. Quan, J.F. Zheng, D. Wang, Probing the interphase "HO• zone" originated by carbon nanotube during catalytic ozonation, Water Res. 122 (2017) 86–95, https://doi.org/10.1016/j.watres.2017.05.063.
[50] F. Hasanvandian, A. Shokri, M. Moradi, B. Kakavandi, S. Rahman Setayesh, Encapsulation of spinel $CuCo_2O_4$ hollow sphere in V_2O_5-decorated graphitic carbon nitride as high-efficiency double Z-type nanocomposite for levofloxacin photodegradation, J. Hazard Mater. 423 (Pt B) (2022), 127090, https://doi.org/10.1016/j.jhazmat.2021.127090.